Delamination initiation in fully clamped rectangular CFRP laminates subjected to out-of-plane quasi-static indentation loading

Huo, L.; Alderliesten, R.C.; Sadighi, Mojtaba

DOI
10.1016/j.compstruct.2022.116316

Publication date
2022

Document Version
Final published version

Published in
Composite Structures

Composite Structures 303 (2023) 116316

Contents lists available at ScienceDirect

Composite Structures

journal homepage: www.elsevier.com/locate/compstruct

Delamination initiation in fully clamped rectangular CFRP laminates subjected to out-of-plane quasi-static indentation loading

Lubin Huo [a,*], René Alderliesten [a], Mojtaba Sadighi [b]

[a] Structural Integrity & Composites Group, Faculty of Aerospace Engineering, Delft University of Technology, P.O. Box 5058, 2600 GB Delft, the Netherlands
[b] Department of Mechanical Engineering, Amirkabir University of Technology, P.O. Box 15875-4413, Tehran, Iran

ARTICLE INFO

Keywords:
Polymer-matrix composites (PMCs)
Delamination initiation
Finite element analysis (FEA)
Analytical modelling

ABSTRACT

To further investigate the effects of in-plane and out-of-plane stresses on the delamination initiation for composite laminates under out-of-plane loading, this paper reports a joint experimental and numerical study, in which the fully clamped rectangular CFRP composite laminates were subjected to out-of-plane quasi-static indentations. The results show that the combination of the out-of-plane shear and in-plane tensile stresses together determined the initiation of delamination, whereas the influences of the out-of-plane compressive stress on the delamination initiation can be neglected. For the purpose of understanding the effects of deformations on the out-of-plane shear and compressive stress distributions, a concise analytical model was developed, which was validated against the numerical and experimental results. As a key take-away, this study reveals that the common impact tests at the geometric centre of the panel may not resemble sufficient similitude with stiffened panels where panel flexure is suppressed by various geometrical stiffening concepts.

1. Introduction

Fibre reinforced polymer composite laminates are used these days in many engineering applications for their high strength-to-mass and stiffness-to-mass ratios [1–3]. In aeronautics, both Boeing and Airbus have developed a modern commercial aircraft made of carbon fibre reinforced composites up to approximately 50 % of their total mass [4,5]. Despite the evident advantages, the great weakness of composite laminates is their vulnerability to out-of-plane loading, or more specifically to out-of-plane impact or indentation loading, due to the lack of through-thickness reinforcement [6]. This has led to an abundant amount of studies into the damage behaviours of composite laminates under such kind of loading [7–12]. These works showed that the impact/indentation damages are generally a mixture of matrix cracking, delamination, and fibre breakage [13–15], and among those three damage modes, delamination is the major one which have attracted the attention of many researchers [16–20].

It is known that the impact delaminations are triggered by matrix cracks [14], therefore, the initiation of such delaminations is usually referred to as the initiation of these special matrix cracks. In order to properly model/predict the initiation of impact delaminations, a thorough understanding about the initiation driving forces for these special matrix cracks is necessary. Over the past few decades, efforts have been made towards this direction and several delamination initiation criteria have been proposed. Some of these criteria are summarized in Table 1, they are separately adopted/developed by Brewer and Lagace [21] in 1988, by Choi and Chang [22] in 1992, by Hou et al. [23] in 2000, and by Hou et al [24] in 2001.

The major conclusion that can be drawn from Table 1 is that there is still no consensus on exactly which in-plane and out-of-plane stress combination induced the initiation of the delamination. Brewer and Lagace [21] claimed that only the out-of-plane stress components contribute to delamination initiation. Hou et al [24] also supported this view, but they emphasized that delamination cannot initiate from the high normal compressive stress zone, they believed that the out-of-plane compression delayed delamination initiation. In contrast, Choi and Chang [22] and Hou et al. [23] suggested that the in-plane normal stress also contributed to the initiation of delamination, but they did not consider and follow whether the out-of-plane normal stress affects the delamination initiation as well.

Such disagreements about the driving forces for the delamination initiation are essentially attributable to the different stress distribution assumptions adopted by various researchers in the development of their own criteria. Completely overcoming this issue first requires a more

* Corresponding author.
E-mail address: L.Huo@tudelft.nl (L. Huo).

https://doi.org/10.1016/j.compstruct.2022.116316
Received 12 February 2022; Received in revised form 17 August 2022; Accepted 7 October 2022
Available online 13 October 2022

Table 1
Some of the delamination initiation criteria proposed in literature.

Expression	Constraint	Reference
$\left(\frac{\sigma_{33}^{+}}{Z_T}\right)^2+\left(\frac{\sigma_{33}^{-}}{Z_C}\right)^2+\left(\frac{\sigma_{13}}{S_{13}}\right)^2+\left(\frac{\sigma_{23}}{S_{23}}\right)^2=1$	–	[21]
$\left(\frac{\sigma_{22}}{Y_T}\right)^2+\left(\frac{\sigma_{23}}{S_{23}}\right)^2=1$	–	[22]
$\left(\frac{\sigma_{22}}{Y_T}\right)^2+\left(\frac{\sigma_{12}}{S_{12}}\right)^2+\left(\frac{\sigma_{23}}{S_{23}}\right)^2=1$	$\sigma_{22}\geq 0$	[23]
$\left(\frac{\sigma_{33}}{Z_T}\right)^2+\frac{\sigma_{23}^2+\sigma_{13}^2}{S_{13}^2}=1$	$\sigma_{33}\geq 0$	[24]
$\frac{\sigma_{23}^2+\sigma_{13}^2-8\sigma_{33}^2}{S_{13}^2}=1$	$-\sqrt{(\sigma_{13}^2+\sigma_{23}^2)/8}\leq\sigma_{33}<0$	[24]
No delamination	$\sigma_{33}\leq-\sqrt{(\sigma_{13}^2+\sigma_{23}^2)/8}$	[24]

Note: some criteria have been simplified for illustrative purposes, the 1-direction is parallel to the fibre direction, 2-direction is in-plane and normal to the fibre direction, and 3-direction is parallel to the out-of-plane direction, S_{ij} ($i=1$, 2, 3, $j=1$, 2, 3, $i\neq j$) are the shear strength parameters, Y and Z are separately the transverse and out-of-plane strength parameters, T and C refer to tension and compression, respectively, '+' means tensile stress, whereas '-' for compressive stress.

direct way to correctly determine the stress fields. Then, the clarification of the relationship between the specific stress combination(s) and the initiation of matrix crack which will subsequently trigger delamination becomes possible. To that end, this paper reports a combined experimental and numerical study in which the rectangular multidirectional CFRP composite laminates with four-side clamped boundary conditions were subjected to quasi-static indentations. The choice of quasi-static indentation over impact loading is motivated by the desire to avoid extra signal noise imposed by the dynamic response of device and coupons during the testing. Besides, an analytical model was developed to help understand the relationship between the laminate deformations and stress field distributions.

More specifically, multiple indentations were applied to the clamped laminates following a pattern covering the entire plate to effectively measure the critical indentation force for the delamination initiation and to identify a key parameter for the development of the analytical model. With the measured critical force, several specimens were indented once at their geometric centre to create a damage state that closest to the case where the delaminations just initiate. Ultrasonic C-scanning and optical microscopy were utilized to establish the damage state post-mortem. For the single central indented composite laminates, finite element analysis in ABAQUS which considered damage-induced material property degradations were used to determine the indentation stress fields, to be related to the experimental damage observed.

2. FE model and quasi-static indentation test

2.1. FE model

With current stress measurement techniques, it is impossible to directly measure the stress field of the indented composite laminates. Alternatively, a calibrated finite element (FE) model can be implemented as a stress meter to determine the stress field distribution. The specific steps are then:

- Determine the critical indentation force for delamination initiation experimentally.
- Obtain the coordinates where delamination onset is observed experimentally.
- Measure the stresses numerically: by tracking point with the same coordinates in the calibrated FE model.
- Evaluate the effect of in-plane and out-of-plane stresses on the initiation of delamination by using the material failure theories, for example, the well-known maximum principal stress theory.

In this work, an M30SC/DT120 carbon/epoxy composite laminate with the dimension 150 mm × 300 mm × 2.5 mm and a quasi-isotropic layup sequence $[45/0/-45/90]_{2s}$ is used for the modelling. This FE model considered geometric nonlinearity. All degrees of freedom are constrained for the regions close the plate edges and dimensions of these constrained (fixed) regions are shown in Fig. 1 (a), the associated coordinate system is illustrated in Fig. 1 (b). In the analysis, eccentric load cases are evaluated, through four indentation locations and each location was indented once, which are marked as I, II, III, and IV (Fig. 1 (a)), where location I is on the centre of the laminate, and II, III and IV are on the centre-line parallel to the short edge. The reason for choosing these four locations is to improve the computational efficiency, while ensuring that the vital information about the eccentric stress variations can be obtained. Noted that this FE model only considered single indentation, to achieve the simulation goal, four independent FE models are needed in total.

The occurrence of damages in composite laminate may significantly alter the indentation stress field distribution, in order to improve the prediction accuracy, these damages should be properly modelled. Because this work intended to determine the stress field of the laminate at the delamination initiation stage, the indentation damages need to be well considered are matrix cracking and fibre breakage. Consequently, this FE model was applied with a published ABAQUS user defined material subroutine UMAT [25] to account for material stiffness degradation due to matrix cracks and fibre failures. The Puck failure criterion [26] and constant stress exposure gradual stiffness degradation method were coded in that UMAT.

The elastic and strength properties used for simulations are tabulated in Tables 2 and 3, respectively, and the strength parameters were provided by the material supplier. The steel hemispherical indenter with a diameter of 25 mm was assumed as a rigid body. The contact between indenter and CFRP laminate was modelled as a surface-to-surface contact, for which the normal behaviour is set as 'Hard' and tangential behaviour is treated as penalty friction type with a friction coefficient 0.3. A sensitivity study which changed the friction coefficient from 0.2 to 0.4 was conducted, only small variations were found in the simulation force–displacement curves. The thickness of each layer is 0.15 mm and was meshed with C3D8I (8-node linear brick, incompatible models) elements to address potential convergence issues. The contact part of this model is meshed with a higher mesh density than other regions, and the corresponding element size is 2.0 × 2.0 × 0.15 mm. This mesh size was selected due to the mesh sensitivity study (the mesh sizes adopted were 4.0 × 4.0 × 0.15 mm, 2.0 × 2.0 × 0.15 mm, and 1.0 × 1.0 × 0.15 mm) has shown that with this mesh size the computational time was minimal and simulation result (i.e. the force–displacement curve) was close to the cases which with higher mesh density.

2.2. Quasi-static indentation test

The quasi-static indention test had three purposes: to validate plate deflection predicted by the FE model, to introduce damages into the laminate, and to determine a critical parameter for the analytical stress prediction model. The force–displacement curves obtained during the test were compared with the curves predicted with the FE model. When these two curves have similar curvatures, the absolute value error had to less than 10 %.

2.2.1. Material and test fixture

To be consistent with the FE model, the CFRP panels were made by hand-lay-up using unidirectional carbon/epoxy prepreg M30SC/DT120 supplied by Delta-Tech S. p. a. After hand layup, the panels were put in an autoclave and cured for 90 min with a temperature of 120 ℃ under a

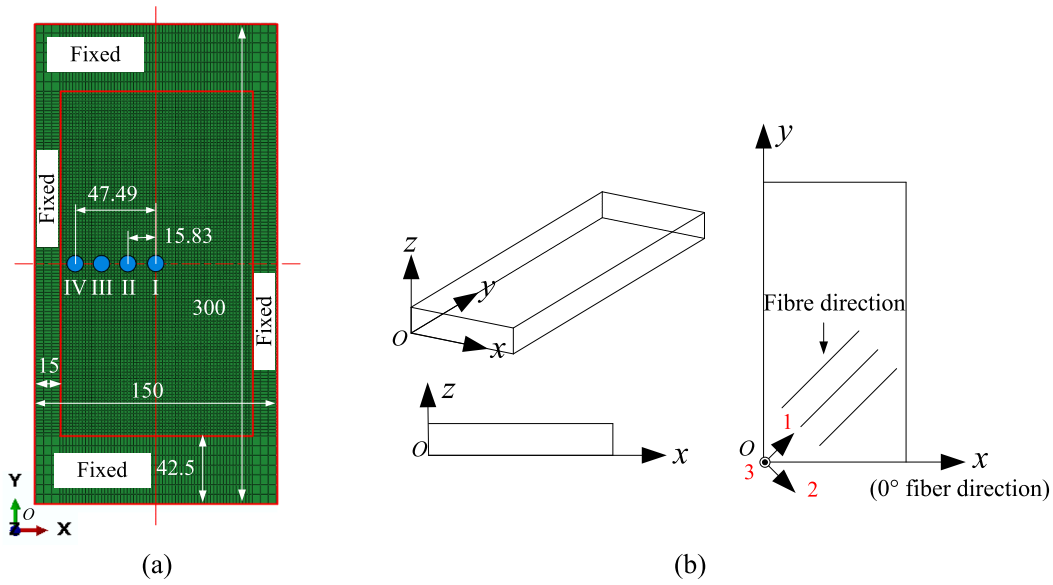

Fig. 1. (a) Panel dimensions of the FE model to calculate single central and eccentric indentation stress fields, (b) coordinate systems used in this study: global coordinate system (black *x*-*y*-*z*) and local coordinate system (red 1–2–3). (For interpretation of the references to colour in this figure legend, the reader is referred to the web version of this article.)

Table 2
Elastic material properties for M30SC/DT120 composite laminate [27].

Density	$\rho = 1.76$ g/cm^3
Young's modulus	$E_{11} = 155$ GPa, $E_{22} = E_{33} = 7.8$ GPa, $G_{12} = G_{13} = 5.5$ GPa, $G_{23} = 3.25$ GPa*
Poisson's ratio	$\nu_{12} = \nu_{13} = 0.27$, $\nu_{23} = 0.2$*

* Value is estimated.

Table 3
Unidirectional laminate strengths of M30SC/DT120 composite (quasi-static loading condition).

Strength	Test method	Test result [MPa]
X_T	ASTM D 3039	3010
X_C	ASTM D 6641	1020
Y_T	ASTM D 3039	39
Y_C	ASTM D 6641	138.0
Z_T*		39
S_{12}	EN 6031	95.6
S_{13} (S_{23})	EN 2563	77.2

* Value is estimated according to Y_T.

pressure of 6 bar. After curing, the panels were cut with a diamond saw to the final dimensions of the specimen: 150 mm × 300 mm, while the nominal thickness is 2.5 mm, with a quasi-isotropic layup sequence $[45/0/-45/90]_{2s}$, where the 0° fibres are aligned along the short edge of the specimen. Prior to testing, all specimens were ultrasonically C-scanned, those without defects were used for the tests.

Since the test fixture recommended by the ASTM standards D7136/D7136M-20 [28] and D6264/D6264M-17 [29] cannot provide a boundary condition like that of the FE model, a new test clamp was designed, which is illustrated in Fig. 2 (a). With this fixture, the short edges of the plate were clamped with the use of bolts, while the other two long edges were clamped by friction induced by high clamping pressure only. The boundary conditions imposed by stiffeners in a stiffened are captured with this test fixture as suggested by Verstraeten [30].

2.2.2. Test details

A Zwick Roell 20 kN servo-hydraulic test machine was used to conduct the quasi-static indentation tests, which is schematically shown in Fig. 2 (b). The out-of-plane indentation load was applied with a 25 mm diameter hemispherical steel nose on the top surfaces of the specimens according to the indentation pattern illustrated in Fig. 2 (c). The distance between any two adjacent locations is 15.83 mm. The force–displacement signals were recorded directly through the transducer. For the multiple indented specimens, the indentations started with position #01, and proceeded in sequence until #91. Each site was indented once with a constant indentation rate of 15 mm/min. Whereas for the single indented specimens, only their geometric centres (i.e. position #46) were indented once at the same loading rate. The indentation tests were executed in displacement control and each indentation was applied up to a predefined indentation force, after which the specimens were unloaded. In this paper, the predefined indentation forces for different specimens were 1500, 2000, and 2500 N, respectively. The test details are tabulated in Table 4.

2.2.3. Damage detections

To obtain information on the state of damages in the laminates, non-destructive and destructive damage inspections were conducted. The projected delamination areas were obtained through ultrasonic C-scanning, after which the specimens were sectioned along the cutting path illustrated in Fig. 2 (c) to ensure that locations #43, #44, #45, and #46 were cut. These four sites correspond to the locations I, II, III, and IV in the FE model (see Fig. 1 (a)). Subsequently, the damage cross-sections were ground with sandpapers with grain sizes of 82, 46.2, 18, 8, and 5 μm successively. Afterwards, the samples were polished with diamond pastes. Finally, the cross-sectional damage images were obtained through the KEYENCE laser microscope with 5 times magnification and then were post-processed through the AutoCAD 2021 software for illustrating purposes.

3. Results and discussion

3.1. FE model validation and verification

To validate the FE model, the predicted force–displacement curve at the indentation location of I (see Fig. 1 (a)) was compared with that of the single central indented composite laminate, as shown in Fig. 3, following the validation practice adopted by many researchers, such as

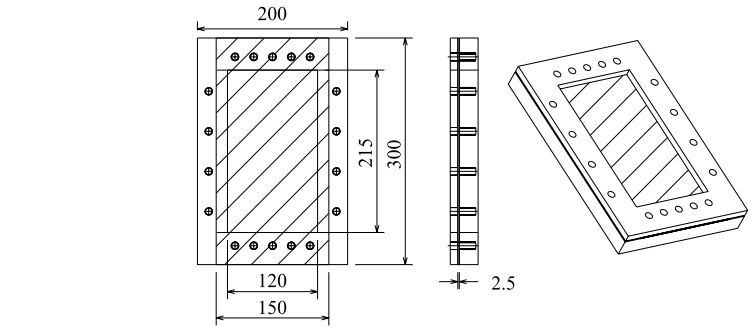

(a) Test clamp. Test specimen clamped in indicated by the hatched area

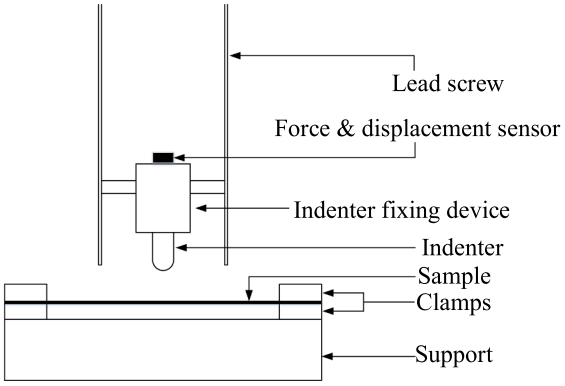

(b) Illustration of the test device

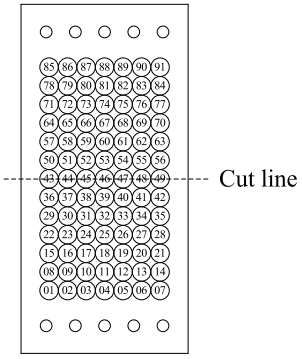

(c) Illustration of the indentation and cutting plans, the distance between two adjacent indentation locations is 15.83 mm

Fig. 2. Details of the quasi-static indentation test.

Table 4
Test matrix.

Test	Number of specimens	Predefined indentation force [N]	Indentation sequence
QSI_01	1	1500	From #01 to #91
QSI_02	1	2000	From #01 to #91
QSI_03	1	2500	From #01 to #91
QSI_04	3	2500	#46 (single indentation)

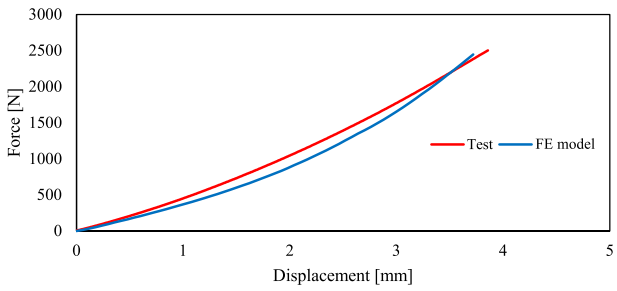

Fig. 3. Comparison between the FE model predicted force–displacement curve with that of the single central indented test, the indentation location was I (Fig. 1(a)) for the FE model and #46 (Fig. 2 (c)) for the specimen.

[31–34]. The correlation demonstrated that the simulation curve is in a good agreement with that obtained from the tests, both in curvature and absolute values. The difference may be attributed to the simplifications that made in the development of the FE model, such as the simplification in contact between the indenter and plate, and no plastic deformations were considered for the matrix.

To further demonstrate the validity of the FE results, the distribution of the out-of-plane normal stress along the thickness predicted with the FE model is shown in Fig. 4 (the associated Cartesian coordinate system is shown in Fig. 1 (b)). The variation of the out-of-plane normal stress was then compared with Talagani's analytical model which had been proven to be capable of predicting the distribution of the out-of-plane normal stress in the thickness direction within the contact zone of a single central indented multidirectional composite laminate. Fig. 4 shows that FE and the analytical results are fit quite well, combined with the reasonable plate indentation response approximation, the authors

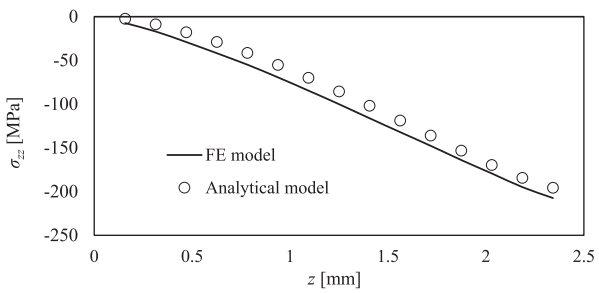

Fig. 4. Comparison of the distribution of the out-of-plane normal stress σ_{zz} along the thickness direction of the laminate directly beneath the indenter predicted with the FE model and analytical model [35] at position I as show in Fig. 1 (a) (# 46 in Fig. 2 (c)), under an indentation force of 2500 N.

believe that this model can correctly predict the stress field of the composite laminates under the quasi-static indentation loading.

3.2. Delamination initiation stage determined by ultrasonic C-scan

To determine the load level at which delaminations just initiate, the C-scan images from the experiments were evaluated. Once the critical delamination initiation load level was determined, the delamination initiation stress state of the laminate was established using the FE model. The relationship between the initiation of delamination and specific stress combinations was obtained through comparing the cross-sectional damage morphologies with the stress field.

The C-scan images are given in Fig. 5, illustrating that under the indentation load of 1500 N, no damages were observed, while for the laminate under the indentation load of 2000 N, damages initiated in the areas close to the clamped edges. For the indentation load of 2500 N, more damages developed in other areas, whereas the damages near the clamped edge merged into larger ones. This means that under the load level of 2000 N, damages started to form in the clamped edge area, while for other regions, the corresponding indentation load is near 2500 N.

An interesting point learned from the C-scan results is that the minimum indentation load that is required for initiation of damage is not identical for all locations. In general, the area close to the clamped edge is more susceptible to damage formation than other areas. The implication of this observation for studying cross-sectional damages was that only the plate loaded by the indentation load of 2500 N could be used, to ensure that the central areas of the composite laminates are at damage initiation stage.

3.3. Stress state corresponding to delamination initiation

To further assess the effect of in-plane and out-plane stresses on the initiation of delamination, the stress state at the point where delamination nucleation just occurs should be fully understood. Fig. 6 illustrates the basic feature of most of the delaminations observed in this study, i.e. the matrix cracks connected to the delaminations have a 45° incline from the normal direction. Moreover, all delaminations nucleate at the layers with 90° fibre orientation: the 9th and 13th layers (labelled L09(90°) and L13(90°)). As a matter of fact, this is a typical delamination initiation mode for a composite laminate under out-of-plane concentrated loading: delamination triggered by matrix crack with fracture planes parallel to the fibre direction [14]. Therefore, in this paper, the initiation of delamination refers to the initiation of the matrix crack which is capable of inducing delamination.

Because Fig. 5 shows that under the indentation force of 2500 N, most of the central area loading points are nearly at delamination

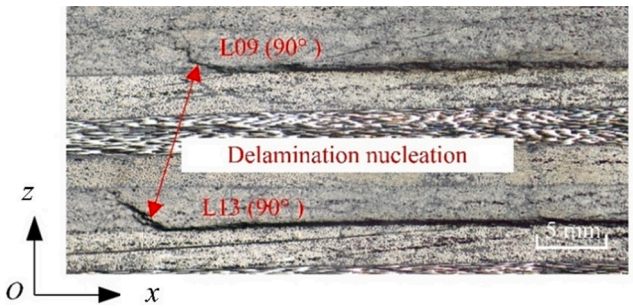

Fig. 6. Typical feature of the indentation delamination nucleation: a 45° incline from the normal direction.

initiation phase, the stresses at the delamination onset points of the single central indented composite laminates with indentation force of 2500 N were obtained through the FE model and were summarized in Table 5, and their standard deviations were given in Table 6. The indentation damages in the multiple indentations case were not considered, mainly due to the neighbouring damages caused by the previous indentations may affect the considered stress field distributions, and the present FE model failed to account for such potential influences. In addition, it should be noted that, as illustrated in Fig. 7, the delamination initiation stress state is represented by the average stresses of the ply interface nodes of the FE model closest to a and b, these two points are the intersections or potential intersections of the intraply crack with the ply interfaces.

Table 5 shows that the stress states corresponding to the onset of delaminations are complex. Note for example that the stress σ_{22} at the delamination initiation points of all 9th layers is close to 0 MPa, whereas their counterparts in all 13th layers are about 31 MPa. Considering that

Table 5
Stress state corresponding to delamination initiation.

Layer	$\bar{\sigma}_{11}$ [MPa]	$\bar{\sigma}_{22}$ [MPa]	$\bar{\sigma}_{33}$ [MPa]	$\lvert\bar{\sigma}_{12}\rvert$ [MPa]	$\lvert\bar{\sigma}_{13}\rvert$ [MPa]	$\lvert\bar{\sigma}_{23}\rvert$ [MPa]
#46_01_L09	145.23	−0.51	−74.72	3.70	0.50	70.19
#46_02_L09	146.66	−0.52	−76.	3.77	0.44	70.27
#46_03_L09	141.35	−0.52	−70.56	3.52	0.62	70.62
#46_01_L13	650.08	32.50	−23.08	3.95	2.27	47.67
#45_02_L13	664.52	33.54	−27.62	4.07	2.02	46.32
#46_03_L13	685.09	34.27	−32.20	4.24	1.51	40.55

Note: the average stress component here refers to the average of the stress of the delamination initiation points at the same interfaces, 01, 02, and 03 are used to mark different specimens.

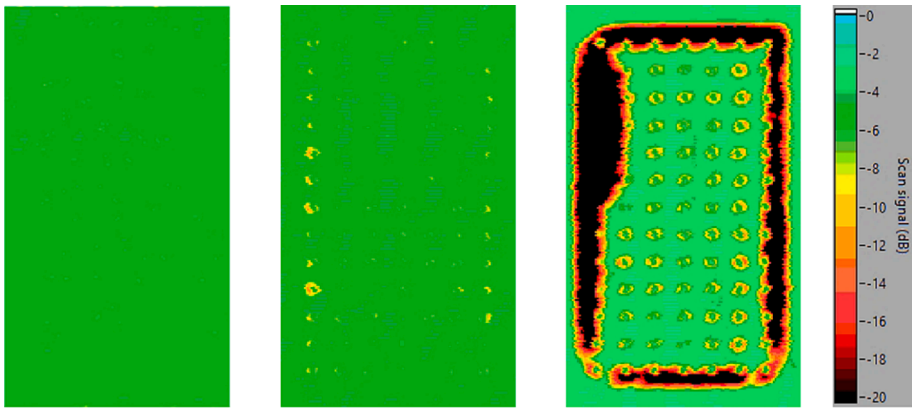

(a) F_{max} = 1500 N (b) F_{max} = 2000 N (c) F_{max} = 2500 N

Fig. 5. C-scan damage images, all 91 loading points in Fig. 2 (c) were indented once, F_{max} refers to the predefined indentation force.

Table 6
Standard deviations for the average stress components.

Layer	$\bar{\sigma}_{11}$ [MPa]	$\bar{\sigma}_{22}$ [MPa]	$\bar{\sigma}_{33}$ [MPa]	$\lvert\bar{\sigma}_{12}\rvert$ [MPa]	$\lvert\bar{\sigma}_{13}\rvert$ [MPa]	$\lvert\bar{\sigma}_{23}\rvert$ [MPa]
#46_01_L09	1.97	0.06	2.32	0.98	0.11	1.06
#46_02_L09	0.54	0.07	0.89	1.05	0.06	1.13
#46_03_L09	4.73	0.00	4.86	0.82	0.23	0.26
#46_01_L13	2.71	0.35	2.55	0.03	0.08	4.55
#45_02_L13	8.34	1.17	6.22	0.07	0.11	5.86
#46_03_L13	22.81	1.52	9.23	0.18	0.51	11.57

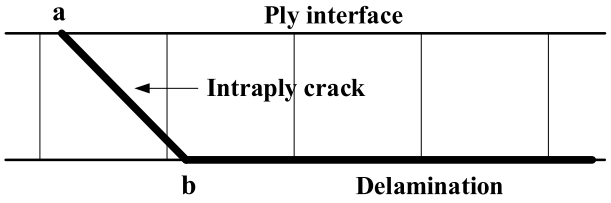

Fig. 7. Illustration of the stress state determination for the delamination initiation point, the stress state is represented by the average stresses of the FE model nodes closest to a and b.

the in-plane normal stress σ_{11} is parallel to the fibre direction, its effect on the initiation of delamination is negligible due to the constraints of fibres. In addition, the out-of-plane shear stress σ_{23} dominates all the shear stress components. Therefore, the stresses potentially contributing to the initiation of delaminations are mainly the in-plane normal stress σ_{22}, out-of-plane normal stress σ_{33}, and out-of-plane shear stress σ_{23}.

To determine which stress led to the initiation of the delamination, all possible combinations of the potential stresses were interpreted with the well-known maximum principal stress theory. These maximum principal stress form stress combinations and their average values of different initiation points at the 9th and 14th layers are summarised in Table 7.

The critical stress combination for the delamination initiation should be equal to the effective delamination initiation threshold, which should just be related to the strength properties of the laminate. For the delaminations in different interfaces, the effective initiation threshold must be the same. Table 7 shows that for all stress combinations, only the combination of σ_{22} and σ_{23} can obtain similar stable values for different layers. The detailed values for the stress combination σ_{22} and σ_{23} at each delamination initiation point is shown in Fig. 8. Fig. 8 shows

Table 7
Maximum principal stress form combinations of the potential stresses for the delamination initiation.

Potential stress combinations for delamination initiation	Average of the maximum normal stresses [MPa]	
	Layer_09	Layer_13
$\sigma_{22}/2+\sqrt{(\sigma_{22}/2)^2}$	0.00 (0.00)	33.43 (1.33)
$\sigma_{33}/2+\sqrt{(\sigma_{33}/2)^2}$	0.00 (0.00)	0.00 (0.00)
$\sqrt{\sigma_{23}^2}$	70.36 (0.93)	44.65 (8.63)
$\sigma_{22}/2+\sqrt{(\sigma_{22}/2)^2+\sigma_{23}^2}$	70.10 (0.90)	64.55 (7.07)
$\sigma_{33}/2+\sqrt{(\sigma_{33}/2)^2+\sigma_{23}^2}$	42.57 (1.67)	33.38 (10.40)
$(\sigma_{22}+\sigma_{33})/2+\sqrt{[(\sigma_{22}-\sigma_{33})/2]^2}$	−0.52 (0.05)	33.43 (1.33)
$(\sigma_{22}+\sigma_{33})/2+\sqrt{[(\sigma_{22}-\sigma_{33})/2]^2+\sigma_{23}^2}$	42.19 (1.65)	57.69 (7.14)

Note: the number combination refers to *average value (standard deviation)*, e.g. 33.43 (1.33) means that the average maximum principal stress is 33.43 MPa and corresponding standard deviation is 1.33.

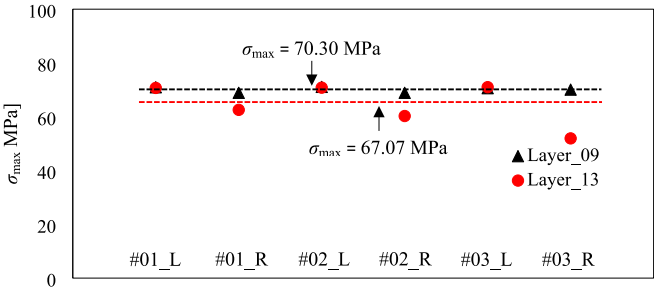

Fig. 8. Combination of the out-of-plane shear and in-plane tensile stresses (σ_{22} and σ_{23}) interpreted with the maximum principal stress theory, $\sigma_{max} = \sigma_{22}/2 + \sqrt{(\sigma_{22}/2)^2+\sigma_{23}^2}$, L and R mean left and right, the loading condition was single central indentation (the loading point is #46 in Fig. 2 (c)) with indentation force of 2500 N, #01, #02, and #03 are used to distinguish different specimens.

that the stable value for most of the delaminations is about 68.69 MPa (i.e. the mean value of all data points excluding #03_R_Layer_13), which is close to the interlaminar shear strength of the unidirectional CFRP laminates made from M30SC/DT120 (Table 3). Therefore, the physical meaning of that stable value is suggested as the interlaminar shear strength of the unidirectional laminate.

In short, the initiation of delamination is driven by the combination of the in-plane tensile and out-of-plane shear stresses (σ_{22} and σ_{23}). The results shown in Table 7 and Fig. 8 demonstrate that the out-of-plane normal stress (σ_{33}) have negligible effects on the initiation of delaminations. Joshi and Sun [36] performed an analytical stress analysis on composites under low velocity impact, and they also suggested that out-of-plane normal stresses were insignificant in the delamination initiation. Although Choi et al. [37] believed that the out-of-plane normal stress can be neglected owning to its value is very small.

3.4. Role of the out-of-plane compressive stress in the formation of delamination

In general, delamination formation consists of delamination initiation and its propagation. In the above section, it has been demonstrated that the out-of-plane compressive stress has negligible effect on the delamination initiation. To illustrate its influence on the delamination propagation, the correlation between the post-processed cross-sectional damages of indentation locations #43, #44, #45, and #46 and distribution of σ_{33} predicted by the FE model are shown in Fig. 9. The results show that just beneath the contact area, the normal compression induced high negative σ_{33}, delaminations and other damages were observed in the regions where σ_{33} became less negative or even positive. This indicates that high negative σ_{33} can prevent the propagation of delamination or delamination cannot propagate in the high normal compression zone.

3.5. Comparison of the delamination lengths at different locations of loading

The total delamination lengths on the right and left sides of the centreline of the damaged cross-sections which are shown in Fig. 9 were measured and plotted in Fig. 10. This figure shows that, in general, when the plate is loaded eccentrically, it produces critical damages at the side closest to the edges, compared to the centre load case, especially for the load location closest to the clamped edge. The delamination lengths on the other side show less of such trend. That is, under the same load level, the damage in the centre of the laminate smaller than the off-centre cases, especially for the areas nearest to the clamped edge. This suggests that the damage size caused by central loading ends up unconservative relative to the eccentric locations where the clamped edge suppresses flexure. Therefore, the common impact tests at the center of

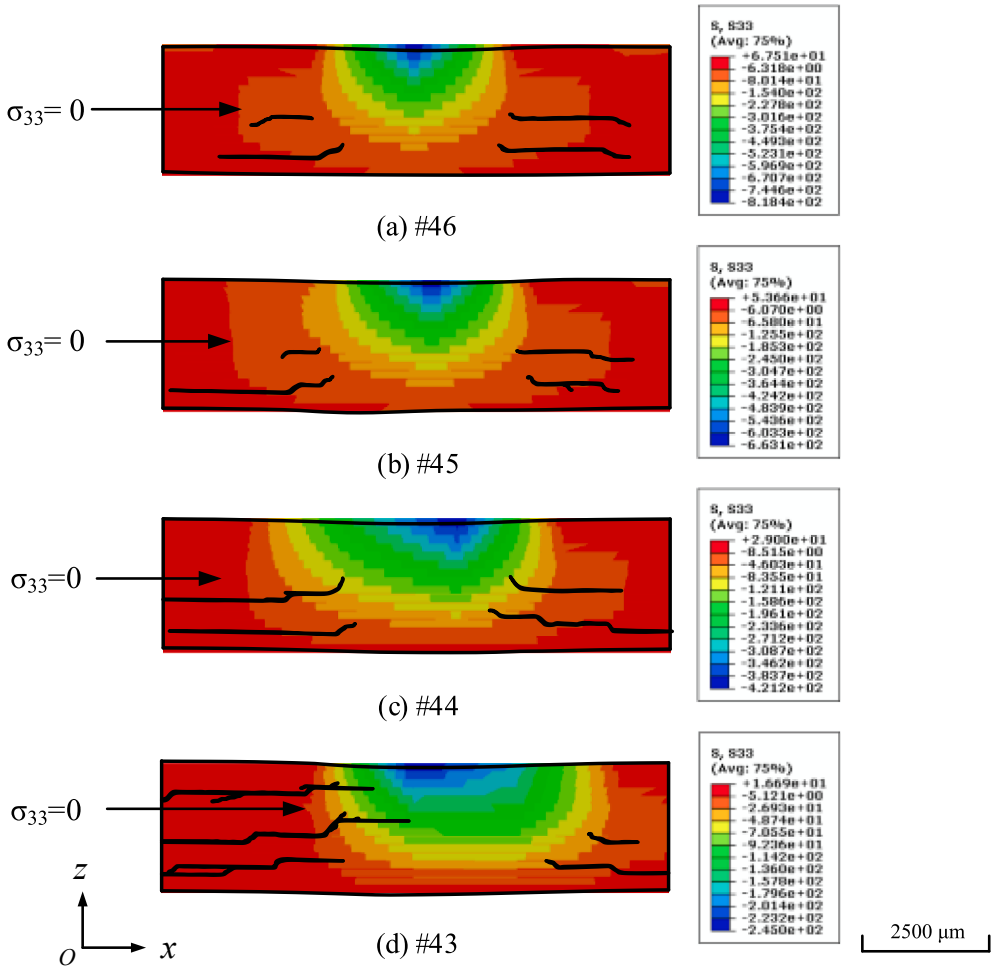

Fig. 9. Correlation between the post-processed cross-sectional damages and distribution of σ_{33} predicted by the FE model.

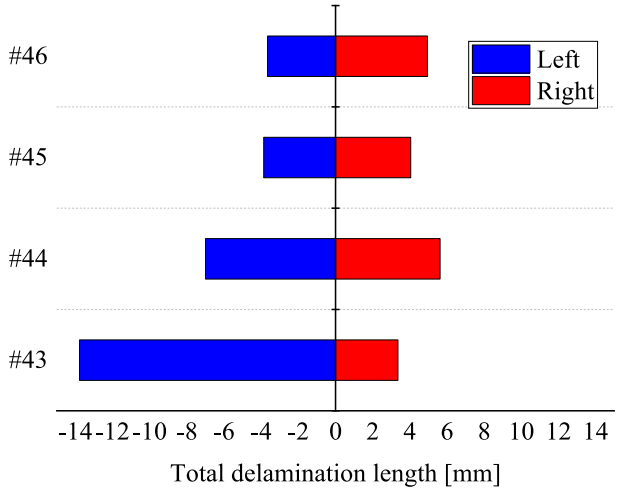

Fig. 10. Total delamination length variations of different indentation locations; note that the location close to the clamped edge #43, produces delaminations twice the length of that at the laminate centre #46.

the panel may not resemble sufficient similitude with stiffened panels where panel deflection is supressed by various geometrical stiffening concepts.

3.6. Analytical model used to elucidate the underlying cause of the out-of-plane stress

The results presented in the above sections show that the out-of-plane stresses are crucial for the formation of delamination. To understand the underlying causes of out-of-plane stresses, an analytical model was developed, which predicts the stress variations (σ_{13} and σ_{33}) in the mid-plane of the laminate along the specific directions.

In general, the stresses in a plate are induced by the combination of various deformations. For a plate under out-of-plane loading, this deformation combination refers to deflection. Besides, the composite laminate used in this study can be defined as thin plate according to the laminated plate theory [38], due to its aspect ratio is 120, which belongs to the thin plate category as it suggested. Considering that the deflection of a thin plate generally consists of global bending deformation and contact induced local contact deformation [39], the deviation of this analytical model should consider these two deformations appropriately. Further, some assumptions have to be made to enable the derivation of such a model, and the analytical model is based on the following assumptions:

- The indenter is assumed as rigid body, which is reasonable for a steel indenter considering that the hardness of the steel is much larger than that of the CFRP laminate.
- The local contact deformation of the plate is symmetric about the central line of the contact area, which is acceptable except for load locations closest to the clamped edge.

– The contact between the hemispherical steel indenter and CFRP laminate is treated as Herzian contact type.
– The coupling effect of the global and local contact deformations on the formation of stress field is not considered, the stresses caused by global and local contact deformations are treated independent of each other.
– The out-of-plane concentrated load is assumed as point load, which is acceptable due to the contact area is negligible compared to the plate dimensions.

3.6.1. σ_{13} and σ_{33} induced by global deformation

The global deformation of the plate can be represented by the mid-plane deflection $w(x,y)$. For a fully clamped orthotropic rectangular thin plate with length a and width b, as illustrated in Fig. 11, subjected to eccentric load at point $(\alpha a, \beta b)$, where $0 \le \alpha \le 1$, $0 \le \beta \le 1$ are the location control parameters, its deflection can be expressed as [40]

$$w(x,y) = \frac{4}{ab}\sum_{m=1}^{\infty}\sum_{n=1}^{\infty} w_{mn}(\sin\alpha_m x)(\sin\beta_n y),\ \ (m=1,2,\ldots,n=1,2,\ldots) \tag{1}$$

where w_{mn} are the coefficients to be determined, and $\alpha_m = m\pi a^{-1}$ and $\beta m = n\pi b^{-1}$.

The relation between the applied point load q and mid-plane deflection $w(x,y)$ can be represented as [41,42]

$$D_x\frac{\partial^4 w}{\partial x^4} + 2H\frac{\partial^4 w}{\partial x^2\partial y^2} + D_y\frac{\partial^4 w}{\partial y^4} = q \tag{2}$$

where D_x and D_y are the flexural rigidities and D_{xy} the torsional rigidity, and H is the effective torsional rigidity, the detailed explanations about these parameters can be found in [40].

The out-of-plane load is assumed to be a point load, that is, the loads applied at the points other than the loading point are considered to be zero, thus, the load, q, can be expressed as

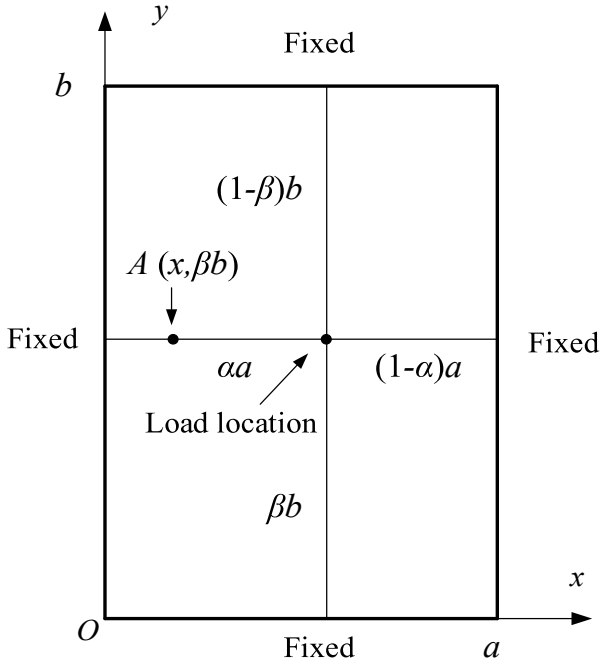

Fig. 11. Definition of dimensions of fully clamped orthotropic rectangular plate under eccentric point load application, where A is any point on the path $y = \beta b$.

$$q = \begin{cases} C & x = \alpha a,\ \ y = \beta b; \\ 0 & x \ne \alpha a,\ \ y \ne \beta b. \end{cases} \tag{3}$$

In addition, the relation between the out of plane shear force V_x (see Fig. 12) and mid-plane deflection $w(x,y)$ can be represented as

$$V_x = -\frac{\partial}{\partial x}\left[\frac{D_1}{v_2}\frac{\partial^2 w}{\partial x^2} + \left(D_1 + 2D_{xy}\right)\frac{\partial^2 w}{\partial y^2}\right] \tag{4}$$

For any point A on the path $y = \beta b$ (Fig. 11), Eq. (2) can be rewritten as

$$w(x,\beta b) = \frac{4}{ab}\sum_{m=1}^{\infty}\sum_{n=1}^{\infty} A_n w_{mn}(\sin\alpha_m x) \tag{5}$$

$w(x, \beta b)$ is only the function of x, thus, the expression of Eqs. (2) and (4) can be reduced to

$$\frac{D_1}{v_2}\frac{\partial^4 w}{\partial x^4} = q \tag{6}$$

$$V_x = -\frac{D_1}{v_2}\frac{\partial^3 w}{\partial x^3} \tag{7}$$

Therefore, the general expression of V_x can be obtained by integrating Eq. (6), following

$$V_x = -\int q dx \tag{8}$$

By substituting the point load defined in Eq. (3) into Eq. (8), the general expression of shear force V_x can be obtained

$$V_x = \begin{cases} C_1 & x < \alpha a; \\ -qx + C_2 & x = \alpha a; \\ C_3 & x > \alpha a. \end{cases} \tag{9}$$

Eq. (9) only shows that the distribution of V_x along the path $y = \beta b$ is constant, but the exact distribution cannot be known without measurement. However, this measurement cannot be performed due to the limitations of such technique. A feasible method is to obtain the expression of shear force distribution equivalently through the beam theory. This approximation method will be introduced in detail below.

The path $y = \beta b$ on the four-side clamped plate can be treated as a beam with fixed–fixed boundary condition, for which the two long edges are constrained by adjacent materials. Such constraint of the adjacent materials can be quantified by the deflection difference between this equivalent beam and real fixed–fixed beam. By analogy with the fixed–fixed beam theory, one can obtain and describe the shear force

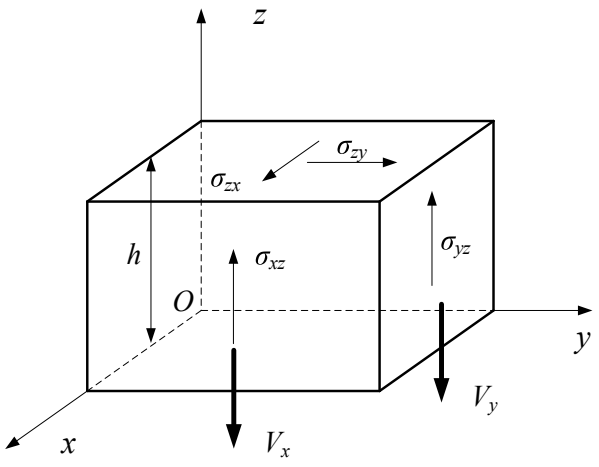

Fig. 12. Out of plane shear forces and out-of-plane shear stresses.

distribution along the path $y = \beta b$ with

$$V_x = \begin{cases} \mu q(1-\alpha)^2(1+2\alpha) & x < \alpha a; \\ 0 & x = \alpha a; \\ -\mu q \alpha^2(3-2\alpha) & x > \alpha a. \end{cases} \tag{10}$$

where μ is the parameter that is used to compromise the deflection difference between the plate and beam, which can be determined by the deflections of the plate and beam at the load point by using

$$\mu = \left[\frac{w_p(x=\alpha a, y=\beta b)}{w_b(x=\alpha a)}\right]^{1.5} \tag{11}$$

In Eq. (11), index p and b refer to plate and beam, respectively, $w_p(x = \alpha a, y = \beta b)$ can be measured through test, and $w_b(x = \alpha a)$ can be obtained through the fixed–fixed beam theory, as

$$w_b(x=\alpha a) = \frac{q\alpha^3(1-\alpha)^3 a^3}{3E_b I} \tag{12}$$

where E_b and I are the Young's modulus and moment of inertia of the beam, respectively.

The out-of-plane shear stress changes parabolically through the thickness of plates as shown in Eq. (13)

$$\sigma_{xz,\ g}(z) = -\frac{6V_x z}{h^2}\left(1-\frac{z}{h}\right) \tag{13}$$

where h is the thickness of the plate (Fig. 12). From Eq. (13) one can deduce that the maximum out-of-plane shear stress occurs at the mid-plane of the plate. Hence, the variations of out-of-plane shear stress on the mid-plane can be represented as

$$\sigma_{13,\ g} = \sigma_{xz,\ g}(x, z = h/2) = -\frac{3V_x}{2h} \tag{14}$$

where index g refers to global deformation.

Since the classical thin plate theory disregard the out-of-plane normal stress, the normal stress caused by global deformation is assumed to be zero

$$\sigma_{zz,\ g} = 0 \tag{15}$$

3.6.2. σ_{13} and σ_{33} induced by local contact deformation

When the indenter and plate start to contact, the local contact deformation can be represented by a simplified model which is illustrated in Fig. 13.

The maximum shear stress along the x direction in the mid-plane can be obtained through the equation represented by

$$\sigma_{xz,\ l}(x, z = h/2)_{max} = \frac{q}{2\pi r h} \tag{16}$$

where r is the radius of the contact area, the index l refers to local contact deformation. This maximum value is reached at the mid-plane region which is closed to the boundary of the contact area, that is, at the locations where $x = \alpha a \pm r$, which are illustrated as dashed lines in Fig. 13. Then, this maximum decrease with $1/x$ away from the contact area [43], and decrease linearly within the contact area. Finally, the shear stress variations in the mid-plane along the x direction can then be expressed as

$$\sigma_{13,\ l} = \sigma_{xz,\ l}(x, z = h/2) = \begin{cases} \dfrac{q}{\pi r h}\dfrac{1}{(-x+\alpha a - r)} & x < \alpha a - r - 1; \\ \dfrac{q}{2\pi r h} & \alpha a - r - 1 \leqslant x \leqslant \alpha a - r; \\ \dfrac{q}{2\pi r^2 h}(\alpha a - x) & \alpha a - r < x < \alpha a + r; \\ -\dfrac{q}{2\pi r h} & \alpha a + r \leqslant x \leqslant \alpha a + r + 1; \\ -\dfrac{q}{2\pi r h}\dfrac{1}{(-x+\alpha a + r)} & x > \alpha a + r + 1. \end{cases} \tag{17}$$

In addition, the contact pressure between the indenter and plate can induce out-of-plane normal stress in the contact region, and the maximum normal stress induced by contact pressure can be calculated using

$$(\sigma_{zz,\ l})_{max} = \frac{3q}{2\pi r^2} \tag{18}$$

and this maximum value is reaches at the point just beneath the indenter. This contact pressure induced normal stress can be assumed to linearly decrease through thickness of the plate and eventually vanishes on the rear surface. Thus, the normal stress in the mid-plane of the plate can be calculated through

$$\sigma_{zz,\ l}(z) = \frac{z}{h}(\sigma_{zz,\ l})_{max} \tag{19}$$

For the distribution of the normal stress along the x direction, one can assume that this stress linearly decreases in the contact area and disappears outside the contact region. According to this assumption, the trend of the normal stress in the mid-plane along the x direction can be expressed as

$$\sigma_{33,\ l} = \sigma_{zz,\ l}(x, z = h/2) = \begin{cases} 0 & x < \alpha a - r; \\ -\dfrac{p_{max}}{2r}(x - \alpha a + r) & \alpha a - r \leqslant x \leqslant \alpha a; \\ \dfrac{p_{max}}{2r}(x - \alpha a - r) & \alpha a \leqslant x \leqslant \alpha a + r; \\ 0 & x > \alpha a + r. \end{cases} \tag{20}$$

Based on the geometric relation shown in Fig. 13, the radius of the contact area r can be represented as

$$r = \sqrt{\varepsilon(2R - \varepsilon)} \tag{21}$$

where R is the radius of the indenter and ε is the depth of the local contact deformation which can be determined by the Herzian contact law as

$$q = k\varepsilon^{1.5} \tag{22}$$

$$k = \frac{4}{3}Q_E\sqrt{R} \tag{23}$$

where Q_E is the effective out-of-plane stiffness and can be decided by using Eq. (24)

$$\frac{1}{Q_E} = \frac{1}{Q_{P3}} + \frac{1}{Q_I} \tag{24}$$

and the indexes P and I refer to the plate and indenter. In Eq. (24), Q_{P3} and Q_I can be decided through the equations shown in Eqs. (25) and (26) respectively

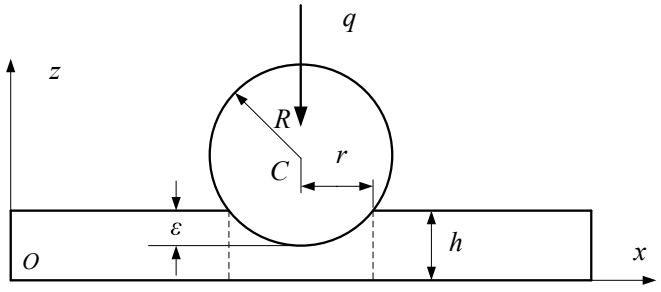

Fig. 13. Illustration of the deformation of the plate due to contact.

$$Q_{P3} = \frac{E_{33}}{(1 - \nu_{13}\nu_{31})} \tag{25}$$

$$Q_I = \frac{E_I}{(1 - \nu_I^2)} \tag{26}$$

where E_{33}, ν_{13}, and ν_{31} are the Young's modulus in the out-of-plane normal direction and corresponding Poisson's ratios of the orthotropic plate, respectively, E_I and ν_I are the Young's modulus and Poisson's ratio of the indenter, respectively.

3.6.3. Analytical model verification

The analytical model can be verified by comparing the predicted stress distributions with those calculated with the FE model without considering damages. Prior to this verification, the compromise parameter μ needs to be determined. To that aim, the multiple indentations were applied following a pattern covering the entire plate front surface, with the same maximum indentation loads of 1500, 2000, and 2500 N, respectively.

Three regions can be identified according to the bending stiffness (i.e. the initial slope of the force–displacement curve [44]):

- Flex (red).
- Medium (green).
- Stiff (cyan).

These three regions are illustrated in Fig. 14. The purpose of classifying these three regions is to facilitate the subsequent analytical model verification.

Based on the test results, μ can be calculated by using Eq. (11) directly. The equivalent beam is approximated as an isotropic one ($E_b = E_{11}$) with a rectangular cross-section, and its moment of inertia can be calculated through $I = ch^3/12$, where c is the width. The recommend value for c is 1 mm in this study, to ensure that the width of the equivalent beam is negligible compare to the dimensions of the plate. Besides, the Young's modulus and Poisson's ratio of the steel indenter are $E_I = 220$ GPa, $\nu_I = 0.28$, respectively, which are acceptable for most carbon and alloy steels [45]. The calculations show that the range of μ is between 0.007 and 1.0, in general, the closer to the clamped edge, the larger the value of μ. The range of μ for different stiffness regions are tabulated in Table 8.

Table 8
Parameter μ in different stiffness regions.

Stiffness region	μ
Flex	0.006–0.007
Medium	0.014–0.021
Stiff	0.15–0.2

After the compromise parameter μ was determined, the stress distribution of each loading point was obtained. The FE results were compared to the analytical ones, to check whether they exhibit a similar trend and whether the absolute value error is less than 10 %. As μ varies in each stiffness region, its average value was adopted: 0.18 for the stiff region, 0.018 for the medium region, and 0.0065 for the flex region. Therefore, the value of μ for #43 is 0.18, for #44 is 0.018, and for #45 and #46 is 0.0065, following their locations in the respective three regions.

Finally, the out-of-plane shear stress variations of those four indentation locations were determined with the analytical model and compared with the simulation results, which are shown in Fig. 15. Fig. 15 illustrates that the analytical model predicted out-of-plane shear stress profiles agree quite well with the FE results for indentations at #44, #45, and #46 (Fig. 15 (a), (b), and (c)). The slight differences in the peak values between these two curves of indentation #46 and left side of indentation #45 are caused by the overestimation of the contact radius in the analytical model. At the right side of indention #43, slight differences in absolute values between the curves can be distinguished: the analytical curve converges to −12 MPa, while the FE curve converges to zero, nonetheless, these two curves still have very similar global curvature. However, this is not the case for the left side of indentation at #43, where the differences in absolute values between the two curves is significant (over 10 %). The fact that qualitatively speaking still some similarities remain, i.e. the curve jumps up towards the clamped area, implies for the stiff region, that the results predicted by the analytical model are at most acceptable from a qualitative perspective.

The out-of-plane normal stress variations at indentations #43, #44, #45, and #46 were obtained with the same procedure as the determination of the out-of-plane shear stress, and the comparisons are shown in Fig. 16. Fig. 16 shows that also here, the analytical results fit very well with the FE results for indentations at #45 and #46. For indentation at #44, the curve peak value predicted by the analytical model is higher than

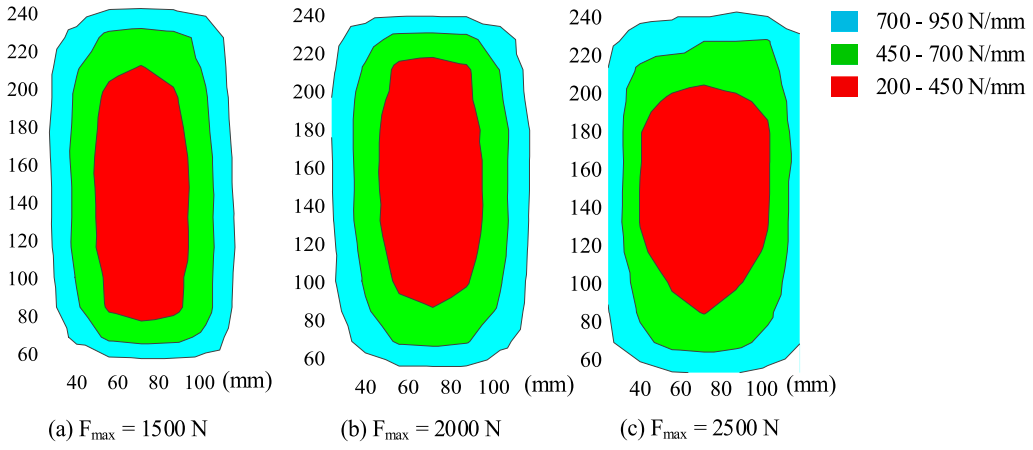

Fig. 14. Illustration of the three typical flexural stiffness regimes as observed in the experimental results: flex (red), medium (green) and stiff (cyan), the dimensions of the images are all in mm, F_{max} refers to the predefined indentation force. (For interpretation of the references to colour in this figure legend, the reader is referred to the web version of this article.)

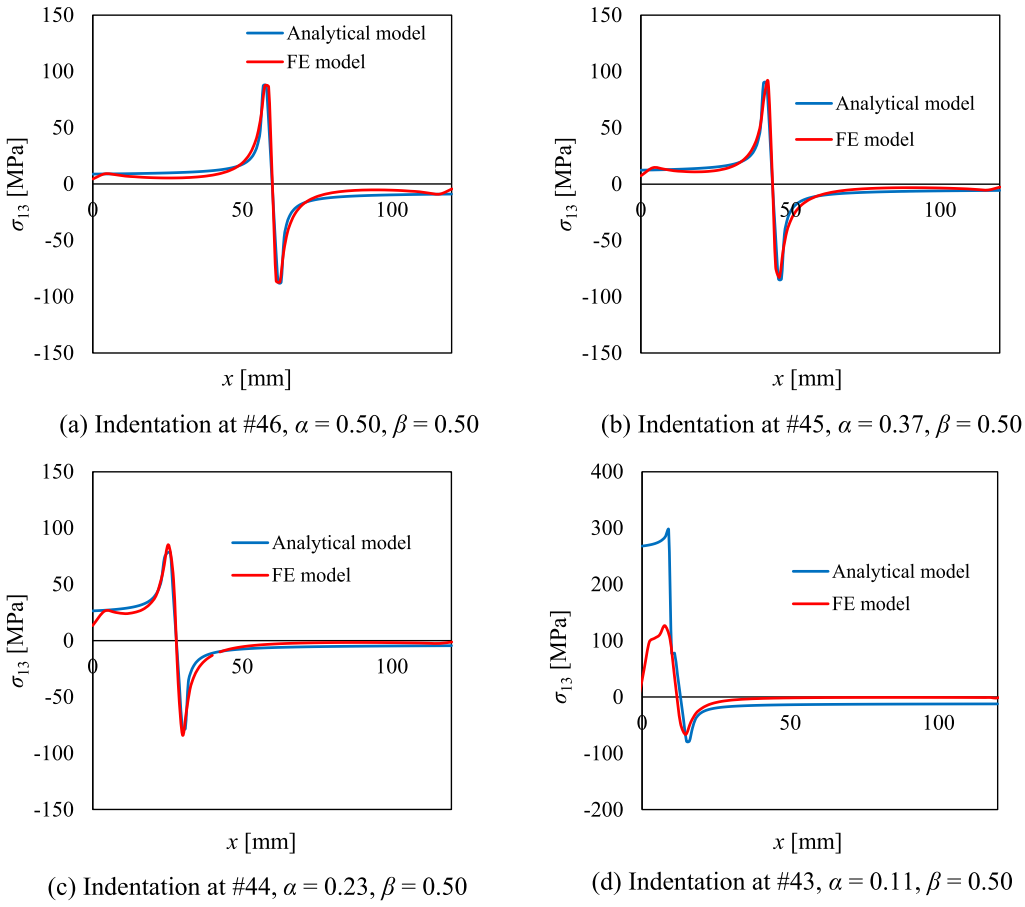

Fig. 15. Comparison of the out-of-plane shear stress variations predicted by the analytical model and FE model for different indentation locations.

that of the FE result. Despite the difference in peak values, the general trend of these two curves is similar. For indentation at #43, however, both the peak value and shape of the analytical curve are hightly different from the FE one, implying that the analytical model failed to predict the out-of-plane normal stress profile in the stiff region. This inability is mainly caused by the local contact deformation induced by contact was assumed to be always symmetrical about the contact area centreline but this assumption is invalid in this case. When the indentation was applied on the plate very close to the clamped edge, the local contact deformation became significantly asymmetric.

In summary, this analytical model can easily predict the stress variations at the mid-plane of the laminates subjected to out-of-plane quasi-static indentation loading, and this derivations also showed that how global bending and local contact deformations relate to the out-of-plane normal and shear stress distributions. Further, the relevant works introduced the principles required for the derivation of analytical stress prediction models for thin laminate. Although the assumptions underneath the model highlighted that the deformation behaviours of thin and thick laminated plates are essentially different, the stress components related to the delamination formation should be similar. Therefore, one can hypothesize in future study that, with these principles, a stress prediction model can be derived for thick composite laminate with extra considerations.

4. Conclusions

The relationship between the specific stress combinations and initiation of delamination of the CFRP laminates subjected to out-of-plane quasi-static indentation loading was investigated. This work demonstrated that the combination of out-of-plane shear and in-plane tensile stresses determined the delamination initiation, whereas the effects of the out-of-plane compressive stress on the delamination initiation can be neglected. The main conclusions are as follows:

- The out-of-plane shear stress and in-plane tensile stress (σ_{23} and σ_{22}) together determined the initiation of delamination for the indented composite laminates. In contrast, the out-of-plane compressive stress ($-\sigma_{33}$) had negligible influences on the delamination initiation. The role of the out-of-plane compressive stress in the formation of delamination is highlighted by the fact that the indentation delaminations cannot propagate in the high normal compression zone.
- An analytical model was developed to assistant understand the underlying causes of the out-of-plane normal and shear stresses. This model was validated with the experimental and numerical results, demonstrating sufficient accuracy for most load locations, except for those much close to the clamped laminate edges. The derivations of this model suggested that the out-of-plane shear stress is caused by the combination of global bending and local contact deformations, whereas the out-of-plane normal stress is only related to the local contact deformation.
- When the laminates were loaded eccentrically, greater damages were formed compared to those which were loaded centrally. Hence, the common impact tests at the centre of the panels may not resemble sufficient similitude with stiffened panels where panel flexure is suppressed by various geometrical stiffening concepts.

CRediT authorship contribution statement

Lubin Huo: Conceptualization, Methodology, Validation, Formal

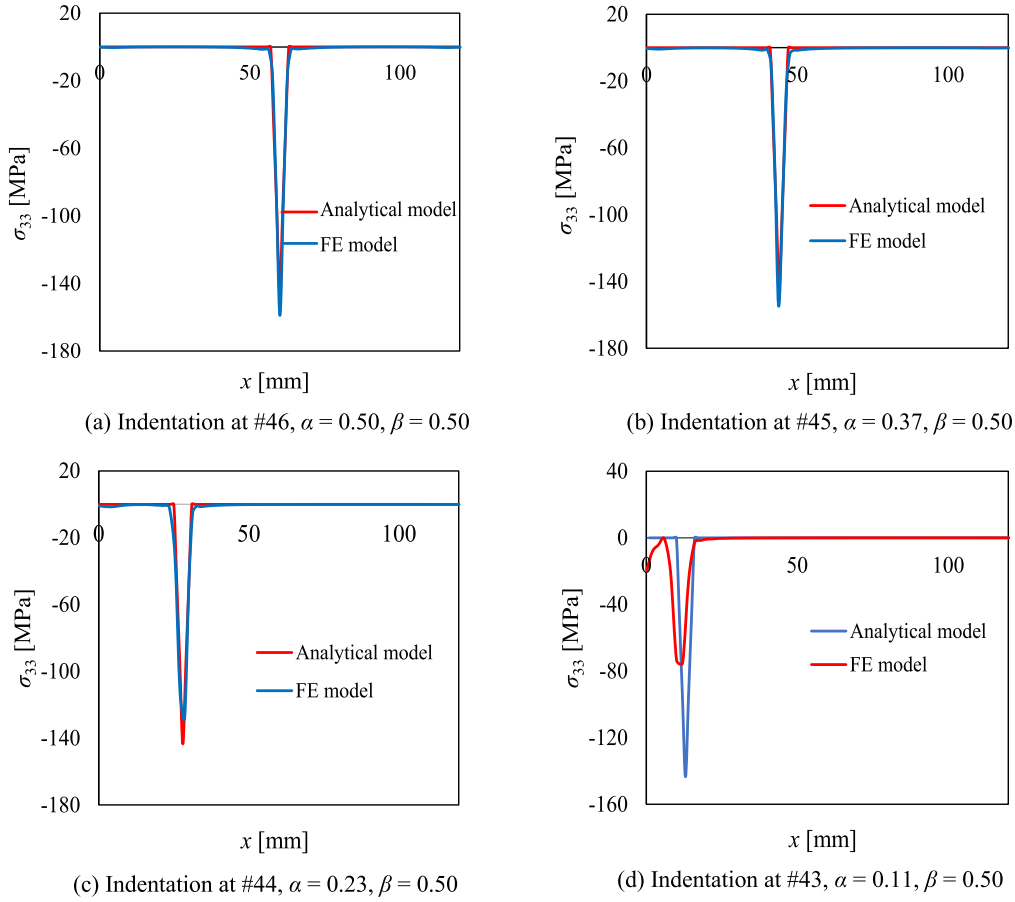

Fig. 16. Comparison of the out-of-plane normal stress variations predicted by the analytical model and FEA model for different indentation locations.

analysis, Investigation, Data curation, Writing – original draft, Writing – review & editing. **René Alderliesten:** Conceptualization, Resources, Writing – review & editing, Supervision, Project administration. **Mojtaba Sadighi:** Writing – review & editing, Supervision.

Declaration of Competing Interest

The authors declare that they have no known competing financial interests or personal relationships that could have appeared to influence the work reported in this paper.

Data availability

Data will be made available on request.

Acknowledgement

The authors gratefully acknowledge the financial support from the China Scholarship Council (No. CSC201806290014). Many thanks to Prof. C. Kassapoglou and Dr. M. R. Talagani for their assistance in the verification and validation of the FE model.

References

[1] Panda HS, Sahu S, Parhi PJT-WS. Effects of moisture on the frequencies of vibration of woven fibre composite doubly curved panels with strip delaminations 2014;78:79–86.
[2] Mohanty J, Sahu SK, Parhi PKJJov, Control. Parametric instability of delaminated composite plates subjected to periodic in-plane loading 2015;21:419–34.
[3] Sahu S, Das PJMS, Processing S. Experimental and numerical studies on vibration of laminated composite beam with transverse multiple cracks 2020;135:106398.
[4] Tang CS, Zimmerman JD, Nelson JI. Managing new product development and supply chain risks: the Boeing 787 case. Supply Chain Forum: Int J: Taylor Francis 2009:74–86.
[5] Herzog D, Schmidt-Lehr M, Canisius M, Oberlander M, Tasche J-P, Emmelmann C. Laser cutting of carbon fiber reinforced plastic using a 30 kW fiber laser. J Laser Appl 2015;27:S28001.
[6] Lewis S. The use of carbon fibre composites on military aircraft. Compos Manuf 1994;5:95–103.
[7] Yashiro S, Ogi K, Yoshimura A, Sakaida Y. Characterization of high-velocity impact damage in CFRP laminates: Part II–Prediction by smoothed particle hydrodynamics. Compos A Appl Sci Manuf 2014;56:308–18.
[8] Breen C, Guild F, Pavier M. Impact of thick CFRP laminates: the effect of impact velocity. Compos A Appl Sci Manuf 2005;36:205–11.
[9] Wagih A, Maimí P, Blanco N, García-Rodríguez S, Guillamet G, Issac R, et al. Improving damage resistance and load capacity of thin-ply laminates using ply clustering and small mismatch angles. Compos A Appl Sci Manuf 2019;117:76–91.
[10] Ghalami-Choobar M, Liaghat G, Sadighi M, Ahmadi HJCS. Eccentric low-velocity impact on fiber-metal laminates under in-plane loading using unified zigzag theory. Compos Struct 2018;201:315–25.
[11] Taherzadeh-Fard A, Liaghat G, Ahmadi H, Razmkhah O, Charandabi SC, Zarezadeh-mehrizi MA, et al. Experimental and numerical investigation of the impact response of elastomer layered fiber metal laminates (EFMLs). Compos Struct 2020;245:112264.
[12] Tarafdar A, Liaghat G, Ahmadi H, Razmkhah O, Charandabi SC, Faraz MR, et al. Quasi-static and low-velocity impact behavior of the bio-inspired hybrid Al/GFRP sandwich tube with hierarchical core: experimental and numerical investigation. Compos Struct 2021;276:114567.
[13] Hull D, Shi YB. Damage mechanism characterization in composite damage tolerance investigations. Compos Struct 1993;23:99–120.
[14] De Moura M, Marques A. Prediction of low velocity impact damage in carbon–epoxy laminates. Compos A Appl Sci Manuf 2002;33:361–8.
[15] Tan W, Falzon BG, Chiu LN, Price M. Predicting low velocity impact damage and Compression-After-Impact (CAI) behaviour of composite laminates. Compos A Appl Sci Manuf 2015;71:212–26.
[16] Elder DJ, Thomson RS, Nguyen MQ, Scott ML. Review of delamination predictive methods for low speed impact of composite laminates. Compos Struct 2004;66:677–83.
[17] Wisnom M. The role of delamination in failure of fibre-reinforced composites. Philos Trans Roy Soc A: Math Phys Eng Sci 2012;370:1850–70.

[18] Schoeppner GA, Abrate S. Delamination threshold loads for low velocity impact on composite laminates. Compos A Appl Sci Manuf 2000;31:903–15.
[19] Hong S, Liu D. On the relationship between impact energy and delamination area. Exp Mech 1989;29:115–20.
[20] Liu D. Impact-induced delamination—a view of bending stiffness mismatching. J Compos Mater 1988;22:674–92.
[21] Brewer JC, Lagace PA. Quadratic stress criterion for initiation of delamination. J Compos Mater 1988;22:1141–55.
[22] Choi HY, Chang F-K. A model for predicting damage in graphite/epoxy laminated composites resulting from low-velocity point impact. J Compos Mater 1992;26:2134–69.
[23] Hou JP, Petrinic N, Ruiz C, Hallett S. Prediction of impact damage in composite plates. Compos Sci Technol 2000;60:273–81.
[24] Hou J, Petrinic N, Ruiz C. A delamination criterion for laminated composites under low-velocity impact. Compos Sci Technol 2001;61:2069–74.
[25] Kodagali K. Progressive failure analysis of composite materials using the puck failure criteria; 2017.
[26] Lee C-S, Kim J-H, Kim S-k, Ryu D-M, Lee J-M. Initial and progressive failure analyses for composite laminates using Puck failure criterion and damage-coupled finite element method. Compos Struct 2015;121:406–19.
[27] Rodi R, Alderliesten R, Benedictus R. Crack-tip behavior in fiber/metal laminates by means of digital-image correlation. J Aircraft 2010;47:1636–46.
[28] ASTM. Standard test method for measuring the damage resistance of a fiber-reinforced polymer matrix composite to a drop-weight impact event. ASTM International 100 Barr Harbor Drive, PO Box C700, West Conshohocken, PA 19428-2959. United States; 2020.
[29] ASTM. Standard test method for measuring the damage resistance of a fiber-reinforced polymer-matrix composite to a concentrated quasi-static indentation force. ASTM International 100 Barr Harbor Drive, PO Box C700, West Conshohocken, PA 19428-2959. United States; 2017.
[30] Verstraeten A. Investigation of low-velocity impacts in multiple impact locations and the effect on its fatigue life. Delft University of Technology; 2019.
[31] Shi Y, Swait T, Soutis C. Modelling damage evolution in composite laminates subjected to low velocity impact. Compos Struct 2012;94:2902–13.
[32] Feng D, Aymerich F. Finite element modelling of damage induced by low-velocity impact on composite laminates. Compos Struct 2014;108:161–71.
[33] Liang S, Liang K, Luo L, Zhang Q, Wang C. Study on low-velocity impact of embedded and co-cured composite damping panels with numerical simulation method. Compos Struct 2014;107:1–10.
[34] Li X, Ma D, Liu H, Tan W, Gong X, Zhang C, et al. Assessment of failure criteria and damage evolution methods for composite laminates under low-velocity impact. Compos Struct 2019;207:727–39.
[35] Talagani MR. Impact analysis of composite structures. 2014.
[36] Joshi S, Sun C. Impact-induced fracture initiation and detailed dynamic stress field in the vicinity of the impact (Retroactive Coverage). American Society for Composites Second Technical Conference; 1987. p. 177–85.
[37] Choi HY, Wu H-Y-T, Chang F-K. A new approach toward understanding damage mechanisms and mechanics of laminated composites due to low-velocity impact: Part II—Analysis. J Compos Mater 1991;25:1012–38.
[38] Steele CR, Balch CD. Introduction to the theory of plates. Division of Mechanics and Computation, Department of Mechanical Engineering Stanford University; 2009.
[39] Olsson R. Impact response of composite laminates: a guide to closed form solutions; 1993.
[40] Li R, Zhong Y, Tian B, Liu Y. On the finite integral transform method for exact bending solutions of fully clamped orthotropic rectangular thin plates. Appl Math Lett 2009;22:1821–7.
[41] Timoshenko S, Woinowsky-Krieger S. Theory of plates and shells; 1959.
[42] Ashwell D. Theory and analysis of plates. Aeronaut J 1975;79:98 -.
[43] Davies G, Zhang X. Impact damage prediction in carbon composite structures. Int J Impact Eng 1995;16:149–70.
[44] Belingardi G, Cavatorta MP, Paolino DS. Repeated impact response of hand lay-up and vacuum infusion thick glass reinforced laminates. Int J Impact Eng 2008;35:609–19.
[45] Gorenc B, Gorenc BE, Tinyou R, Syam A. Steel designers' handbook. UNSW Press; 2005.